Cleaning effects due to shape oscillation of bubbles over a rigid boundary

Corbett, Callan; Wang, Qianxi; Liu, Wenke; Smith, Warren; Walmsley, Damien

DOI:
10.1063/5.0173730

Cleaning effects due to shape oscillation of bubbles over a rigid boundary

Callan Corbett[1], Qianxi Wang[1], Wenke Liu[2], Warren R. Smith[1], and A.D. Walmsley[3]

[1]School of Mathematics, University of Birmingham, Edgbaston, Birmingham, B15 2TT, UK
[2]College of Electronics and Information Engineering, Shenzhen University, Shenzhen, 518061, China
[3]School of Dentistry, College of Medical and Dental Sciences, University of Birmingham, 5 Mill Pool Way, Birmingham, B5 7EG, UK

Abstract

Recent experiments have revealed the interesting cleaning effects that take place due to the shape mode oscillation of bubbles over a rigid boundary. Whilst a microbubble was undertaking shape oscillation moving over a bacterial biofilm, it removed the contaminants from the boundary and created a clean path through the biofilm. This demonstrated much higher cleaning efficiency than that associated with the volume oscillation of cavitation bubbles, however the mechanism is unknown. Here we study this phenomenon using the boundary integral method, with the viscous effects modelled using the viscous potential flow theory and the compressible effects using the weakly compressible theory. The viscous stress at the rigid boundary is approximated using boundary layer theory. We observed that the natural frequencies of shape mode oscillation decrease significantly due to the presence of the boundary. The shear stress at the boundary due to the shape oscillation of a nearby bubble is at least twenty times higher than that due to volume oscillation with the same energy, and is significant only within the area directly beneath the bubble. This is explained by the notably faster decay for higher shape modes of the kinetic energy in the fluid as the distance to the centre of the bubble r increases, with the induced velocity of mode k decaying at a rate of $\mathcal{O}(r^{-(k+2)})$ away from the bubble. These results achieve excellent agreement with the intriguing cleaning effects first observed in the experiment, and explain the mechanism behind this new highly efficient method of cleaning.

1 Introduction

Bubble dynamics has been a central research topic for many decades, providing essential insight into cavitation damage to pumps, turbines, and propellers (Blake and Gibson [1987];

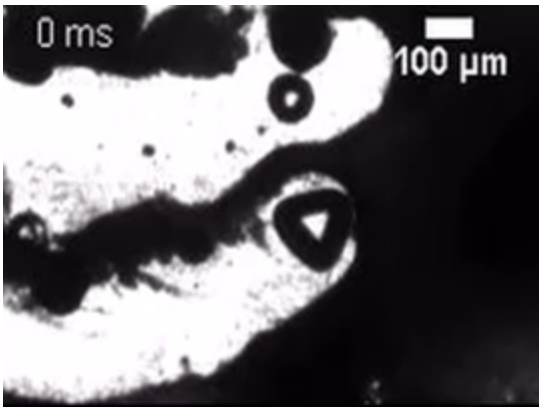

Figure 1: Bubbles on the surface exhibit shape oscillations whilst disrupting the biofilm (Vyas et al. [2020]: supplementary video e).

Lauterborn and Kurz [2010]). Microbubble dynamics subject to an acoustic wave are associated with applications to cavitation cleaning (Ohl et al. [2006]; Chahine et al. [2016]; Reuter et al. [2017]). In practice this has been used to remove bacterial biofilms from dental implants, contaminants from microchips, and aide in the sterilisation of medical instruments (Mason [2016]). This has been attributed to the pressure impulse, the micro-steaming associated with bubble oscillation, and high-speed jetting during bubble collapse (Ohl et al. [2006]; Chahine et al. [2016]; Reuter et al. [2017]).

Recently, Vyas et al. [2020] observed an interesting phenomenon in experiments removing dental biofilms from surfaces using cavitation bubbles generated by a scaler tip vibrating at high frequency. As shown in figure 1, a microbubble in shape mode oscillation directly above a biofilm migrated along the biofilm due to the first Bjerknes force. The shape oscillating bubble removed the contaminating biofilm from the surface and created a clean path through the biofilm, like a brush sweeping away dust. This new phenomenon demonstrated higher cleaning efficiency than that associated with the volume oscillation of microbubbles (Vyas et al. [2020]). This is therefore linked with important applications in ultrasonic cleaning; however, the associated mechanisms are unknown.

There are two important issues to activate and control these applications. Firstly, we need to find the natural frequency of shape modes for a bubble near a rigid boundary. This is because, to activate shape oscillation of bubbles, the driving acoustic wave should be near the natural frequency of shape modes. However, the natural frequency of shape modes has mainly been studied for bubbles in an infinite field. Secondly, it is important to study the cleaning mechanism of a bubble in shape mode oscillation over a boundary, specifically the magnitude and distribution of the shear stress generated at the boundary due to the shape oscillation of the bubble. This is because the mechanism for surface cleaning is the application of shear stress onto contaminants, dislodging them from the surfaces being cleaned. Theoretical studies were undertaken on shape oscillations of bubbles at small amplitudes using perturbation methods via spherical harmonics, predicting the natural frequency of shape modes and the stability threshold (Plesset [1954]; Prosperetti [1977]; Shaw [2009,

2017]; Doinikov [2004]; Guédra et al. [2017], Guédra and Inserra [2018]). It has been noticed that the natural frequency and amplitude of spherical oscillation of bubbles are affected by the presence of a wall (Garbin et al. [2007]; Doinikov and Bouakaz [2010]; Roovers et al. [2019]). Recently, Maksimov [2020] extended the theory for a bubble far away from a flat rigid boundary using the method of images.

To study the above two problems, we describe a numerical model for a bubble in shape mode oscillation near as well as in contact with a rigid boundary, based on the boundary integral method (BIM). The viscous effects are approximated by the viscous potential flow theory (Joseph and Wang [2004]; Wang et al. [2022]) and the compressible effects are modelled using weakly compressible flow theory (Wang and Blake [2010, 2011]). Validation of the model is carried out by comparison with theoretical results (Tsamopoulos and Brown [1983]; Maksimov [2020]). The viscous shear stress at the rigid boundary is then approximated using boundary layer theory (Nyborg [1958]; Doinikov and Bouakaz [2010]). Parametric studies are subsequently carried out for the natural frequency of various shape modes and the shear stress generated at the boundary, in terms of the shape mode and the standoff distance of the bubble from the wall.

2 Viscous compressible BIM model

Consider a bubble near a rigid boundary in a weakly compressible potential flow. Using the weakly compressible theory (Wang and Blake [2010, 2011]), the velocity potential ϕ in the inner region satisfies Laplace's equation, $\nabla^2\phi = 0$. It thus may be represented as a surface integral over the bubble surface S as follows:

$$c(\boldsymbol{r},t)\phi(\boldsymbol{r},t) = \int_S \left(\frac{\partial \phi(\boldsymbol{q})}{\partial n} G(\boldsymbol{r},\boldsymbol{q}) - \phi(\boldsymbol{q}) \frac{\partial G(\boldsymbol{r},\boldsymbol{q})}{\partial n} \right) \mathrm{d}S(\boldsymbol{q}), \tag{2.1}$$

where $\boldsymbol{r}$ is the field point, t is time, $\boldsymbol{q}$ the source point, $c(\boldsymbol{r},t)$ the solid angle, and $\hat{\boldsymbol{n}}$ the unit outward normal at the bubble surface S directed from liquid to gas. To satisfy the impermeable boundary condition on the wall, the Green's function is given as $G(\boldsymbol{r},t) = |\boldsymbol{r}-\boldsymbol{q}|^{-1} + |\boldsymbol{r}-\boldsymbol{q}'|^{-1}$, where $\boldsymbol{q}'$ is the image of $\boldsymbol{q}$ reflected in the wall.

The boundary condition of the potential in the inner region at the far field is (Wang and Manmi [2014], Wang [2016])

$$\phi(\boldsymbol{r},t) = \frac{1}{2\pi c}\ddot{V}(t) \qquad \text{as } |\boldsymbol{r}| \longrightarrow \infty, \tag{2.2}$$

where c is the speed of sound in the liquid, $V(t)$ is the bubble volume at time t, and the over dots denote the derivative in time t.

In the viscous potential flow theory, the dynamic boundary condition at the bubble surface is given as follows:

$$p_L + p_{vc} + \sigma\kappa - 2\mu\frac{\partial^2\phi}{\partial n^2} = p_B, \tag{2.3}$$

where μ is viscosity of the liquid, p_L the liquid pressure at the bubble surface, p_{vc} the viscous pressure correction to be described later, σ surface tension, and κ the local mean curvature

of the bubble surface. The last term on the left-hand side is the normal stress due to viscous effects. We assume the internal pressure p_B of the bubble gas follows the adiabatic law

$$p_B = p_v + p_{g0}\left(\frac{V_0}{V}\right)^{\lambda}, \tag{2.4}$$

where p_v is the vapour pressure, V_0 is the initial volume of the bubble, λ is the ratio of specific heats, and p_{g0} is the initial pressure of the non-condensable bubble gas. We do not consider the thermal effects associated with this phenomenon (Szeri et al. [2003]; Fuster and Montel [2015]). The effects of viscoelasticity were included in the potential flow theory of microbubbles by Lind and Phillips [2010, 2012, 2013].

The viscous pressure correction p_{vc} is given as follows:

$$p_{vc} = -\frac{\boldsymbol{u}_\tau \cdot \boldsymbol{\tau}_s^L}{u_n} \quad \text{on } S, \tag{2.5}$$

where the normal velocity u_n, tangential velocity $\boldsymbol{u}_\tau$ and shear stress $\boldsymbol{\tau}_s^L$ are due to the potential flow. This equation is obtained from the conservation of energy at the bubble surface (Wang et al. [2022]). Classical potential flow theory does not satisfy the conservation of energy at a free surface, rather satisfying the normal stress balance equation. The conservation of energy can be satisfied by adding the pressure correction (2.5) into the normal stress balance equation.

Using the Bernoulli equation, the dynamic boundary condition (2.3) at the bubble surface can be written as

$$\rho\frac{D\phi}{Dt} = p_\infty - p_B + \frac{1}{2}\rho|\nabla\phi|^2 + \sigma\kappa - \frac{1}{2\pi c}\rho\ddot{V} + 2\mu\frac{\partial^2\phi}{\partial n} + p_{vc} \text{ on } S. \tag{2.6}$$

This equation is the same as classical incompressible potential flow theory, except for the last three terms on the right-hand side. The term $\rho\ddot{V}$ reflects the compressible effects of the liquid, and the last two terms represent the weakly viscous effects.

2.1 Modelling a bubble connected to a rigid boundary

When a part of a bubble surface is nearly in contact with the rigid boundary, it tends to remain being nearly in contact with the boundary (Wang et al. [2015]). This results in numerical instabilities in the simulations using the BIM. To avoid these numerical instabilities, we remove the thin layer of liquid between the bubble surface and the boundary, join the bubble surface with its image to the boundary and simulate "the combined bubble" (Ni et al. [2015]; Wang et al. [2015]). In the simulations performed in this paper, the join takes place when the minimum distance δ_{min} between bubble surface and the boundary is in the range of 0.01 to 0.04.

As the bubble surface is in contact with the rigid boundary, the contact angle of the liquid-gas interface with the rigid boundary depends on the properties of the liquid, gas and the hydrophilic property of the boundary and may change with the dynamics (Shikhmurzaev [2007]). For simplicity, we assume that the contact line between them is fixed. With the

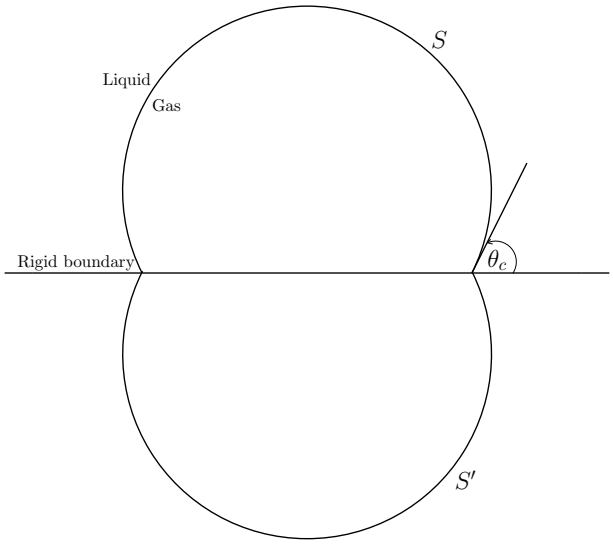

Figure 2: A schematic of a bubble with surface S connected to its image with surface S' on a rigid boundary. The contact angle between the bubble wall and the rigid boundary is θ_c.

smoothed cubic spline used for the interpolation of the bubble surface (Wang et al. [2019]), the solid angle $c(\boldsymbol{r}, t)$ takes the value 2π at the bubble surface except for at the contact line. The solid angle at the point on the contact line is given by

$$c(\boldsymbol{r}, t) = \iint_{S_\varepsilon} \frac{\mathrm{d}S}{\varepsilon^2}, \tag{2.7}$$

where S_ε is the part of a spherical surface with radius ε centred at the contact point, cut by the tangent plane of the bubble surface and the tangent plane of the imaged bubble surface at the contact point. Now,

$$c(\boldsymbol{r}, t) = 2\int_0^{\pi} \mathrm{d}\theta \int_0^{\theta_c} \frac{\varepsilon^2 \sin\phi}{\varepsilon^2}\, \mathrm{d}\phi = 2\pi(1 - \cos\theta_c), \tag{2.8}$$

where θ_c is the angle between the bubble surface and rigid wall at the contact line. This configuration is shown in figure 2.

2.2 Calculating shear stress at the rigid boundary

Nyborg [1958] obtained an approximate solution for the local viscous flow near a rigid boundary due to steady oscillating irrotational flow near a fluid-solid interface using boundary layer theory. The viscous shear stress at the rigid boundary is then approximated using boundary layer theory (Nyborg [1958]; Doinikov and Bouakaz [2010]) by

$$\tau_{zr_2} = \sqrt{\frac{\rho\mu}{\omega}} \left(u_{r2} \frac{\partial u_{r_2}}{\partial r_2} \right)_{z=0} = \sqrt{\frac{\rho\mu}{\omega}} \left(\frac{\partial \phi}{\partial r_2} \frac{\partial^2 \phi}{\partial r_2^2} \right)_{z=0}. \tag{2.9}$$

Here we assume that the z-axis is along the axis of symmetry and the origin is at the rigid boundary; r_2 is the r-coordinate in cylindrical coordinates.

To compare the shear stress for various modes of oscillation, we need to ensure that the bubble system has equal initial energy for each mode. The potential energy of the system is equivalent if the initial radius and bubble gas pressure are kept constant in each case. Thus it remains that the initial kinetic energy of the bubble system must be kept the same.

The kinetic energy of a bubble in a potential flow reads (Wang [2016]):

$$E_k(t) = \frac{\rho}{2} \oint_S \phi \phi_n \, \mathrm{d}S. \tag{2.10}$$

Initially the bubble is spherical, meaning

$$E_k(0) = -\frac{\rho}{2} \oint_S \phi \phi_r \, \mathrm{d}S. \tag{2.11}$$

Assuming the bubble is initially oscillating in shape mode k with amplitude a_k, the initial potential and its derivative with respect to r are given as

$$\phi_k(r,0) = \frac{a_k}{r^{k+1}} P_k(\cos\theta), \quad \frac{\partial \phi_k(r,0)}{\partial r} = -(k+1)\frac{a_k}{r^{k+2}} P_k(\cos\theta). \tag{2.12}$$

Substituting equation 2.12 into 2.11 yields

$$E_k(0) = \frac{\rho}{2}(k+1)\frac{a_k^2}{R_0^{2k+1}} \int_0^{2\pi} P_k^2(\cos\theta) \, \mathrm{d}\theta \int_0^{\pi} \sin\phi \, \mathrm{d}\phi = (k+1)\rho \int_0^{2\pi} P_k^2(\cos\theta) \mathrm{d}\theta, \tag{2.13}$$

where P_n is the Legendre polynomial of order n and R_0 is the initial radius of the bubble. In eqs. (2.11-2.13), (r, ϕ, θ) are the spherical coordinates with the origin at the bubble centre. With suitable choice of the amplitude a_k, the initial kinetic energy of the bubble system can be set at the same value for different modes k. The shape modes $k = 0, 1$ are for the spherical oscillation, translation of a bubble, and $k \geq 2$ is for non-spherical oscillation.

3 Numerical results and discussion

3.1 Validation of BIM model

The ability of the present BIM model to accurately model nonlinear oscillations is demonstrated in figure 3 in a comparison with the analytic results of Tsamopoulos and Brown [1983]. A bubble, initially at equilibrium, with a radius of 0.06 cm is surrounded by an infinite fluid, in this case taken to be water. The density of the surrounding fluid is $\rho = 998$ kg m^{-3}, the viscosity is $\mu = 10^{-3}$ Pa·s, the surface tension coefficient is $\sigma = 0.073$ N m^{-1}, and the polytropic constant is taken to be $\lambda = 1.4$. The ambient pressure is taken as $p_\infty = 101300$ Pa, and the vapour pressure inside the bubble is $p_v = 2980$ Pa. Here, the natural frequency of mode two oscillation is plotted against an increasing amplitude of oscillation measured by the axis ratio at maximum prolate shape (L/W). As the ratio increases, i.e. the

size of the initial disturbance at the surface of the bubble increases, the natural frequency of oscillation decreases at a nonlinear rate. The numerical results of the BIM agree very well up to an axis ratio of $L/W = 1.5$, before starting to diverge from the analytic results. This can be explained by the limitations of the asymptotic model, which is only accurate up to a certain order.

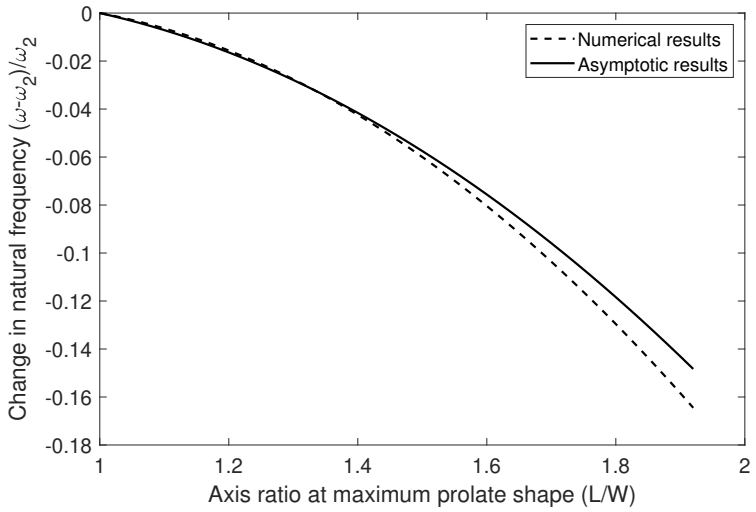

Figure 3: Comparison between change in $n = 2$ oscillation frequency with increasing amplitude of oscillation for the numerical results of the BIM (dashed line), and the analytic results of Tsamopoulos and Brown [1983] (solid line). A bubble with initial equilibrium radius R_0 = 0.06 cm is surrounded by an infinite field of water, with parameters $\gamma = 1.4$, $\sigma = 0.073$ N m^{-1}, $\rho = 998$ g m^{-3}, $\mu = 10^{-3}$ Pa·s, $p_\infty = 101300$ Pa and $p_v = 2980$ Pa.

The ability of the BIM model to numerically calculate the natural frequency of small order shape mode oscillations of a bubble is demonstrated in table 1. The initial bubble has a radius of 25 μm, with the remaining parameters the same as in figure 3. A small perturbation to the initial potential at the surface of the bubble is used to stimulate oscillation. This is of the form $\phi_0 = \varepsilon P_l(\cos\theta)$, where $\varepsilon \ll 1$, l is the shape mode number, P_l the Legendre polynomial of order l, and θ the angle between the position on the bubble surface and the r-axis. This initial potential is small and allows for an accurate comparison with the analytic results. As can be seen from table 1, the error in the calculation of the natural frequency of shape mode oscillation is very low. This demonstrates the ability of the present model to accurately predict the natural frequency of the shape mode oscillation of a bubble.

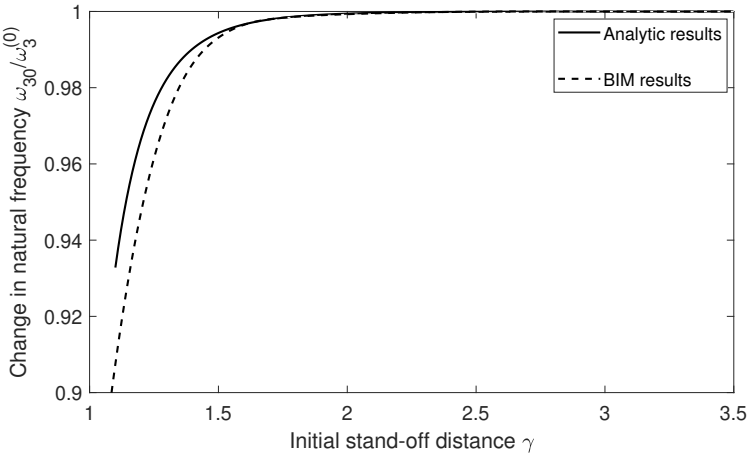

Figure 4: The natural frequency of shape mode three oscillation of a bubble, with initial radius $R_0 = 0.001$ m in water, calculated at multiple stand-off distances γ. The analytic results of Maksimov [2020] are compared with the present BIM model. The remaining parameters are as in figure 3.

Mode number	Analytic natural frequency (Hz)	Numerical natural frequency (Hz)	Error
0	132,395	132,369	0.02%
2	37,684.4	37,710.6	0.07%
3	68,802.1	68,843.0	0.06%
4	103,203	103,329	0.10%

Table 1: Comparison between analytic natural frequency, numerically calculated natural frequency and the associated error for four shape modes of oscillation. The initial radius is 25 μm and the remaining parameters are as in figure 3.

Now, the calculation of natural frequency near to a rigid boundary is compared with the analytic results of Maksimov [2020]. For these analytic results, the natural frequency of shape mode three oscillation of a bubble with initial radius $R_0 = 0.001$ m in water is derived depending on the initial dimensionless stand-off distance to the wall $\gamma = h/R_0$. The effects of surface tension, viscosity, and compressibility are ignored. As axisymmetric shape oscillations are considered, the angular momentum $m = 0$.

As can be seen in figure 4, excellent agreement is achieved between the results of the present BIM and the analytic results as $\gamma \geq 1.5$. As $\gamma \leq 1.5$, the wall effects are significant and are under-predicted by the analytic results. This demonstrates the capability of the BIM to accurately predict the natural frequency of a bubble in the presence of a rigid boundary. Now, these results can be extended to a viscous, compressible fluid, as well as extending the values of the initial stand-off distance that are to be considered.

3.2 Natural frequency of shape mode oscillation for varying stand-off distances

The effects of an increasing stand-off distance on the natural frequency of different shape mode oscillations are detailed in figures 5a-5d. The non-dimensional stand-off distance between the rigid boundary and the centre of the bubble, $\gamma = h/R_0$, is measured against the change in natural frequency of shape mode n, $(\omega - \omega_n)/\omega_n$. Here, ω_n represents the natural frequency of mode n in an infinite fluid. Each case will be using the parameters previously defined in table 1. Volumetric oscillation ($n = 0$) and shape modes two, three and four are considered. Mode one representing translation is not considered.

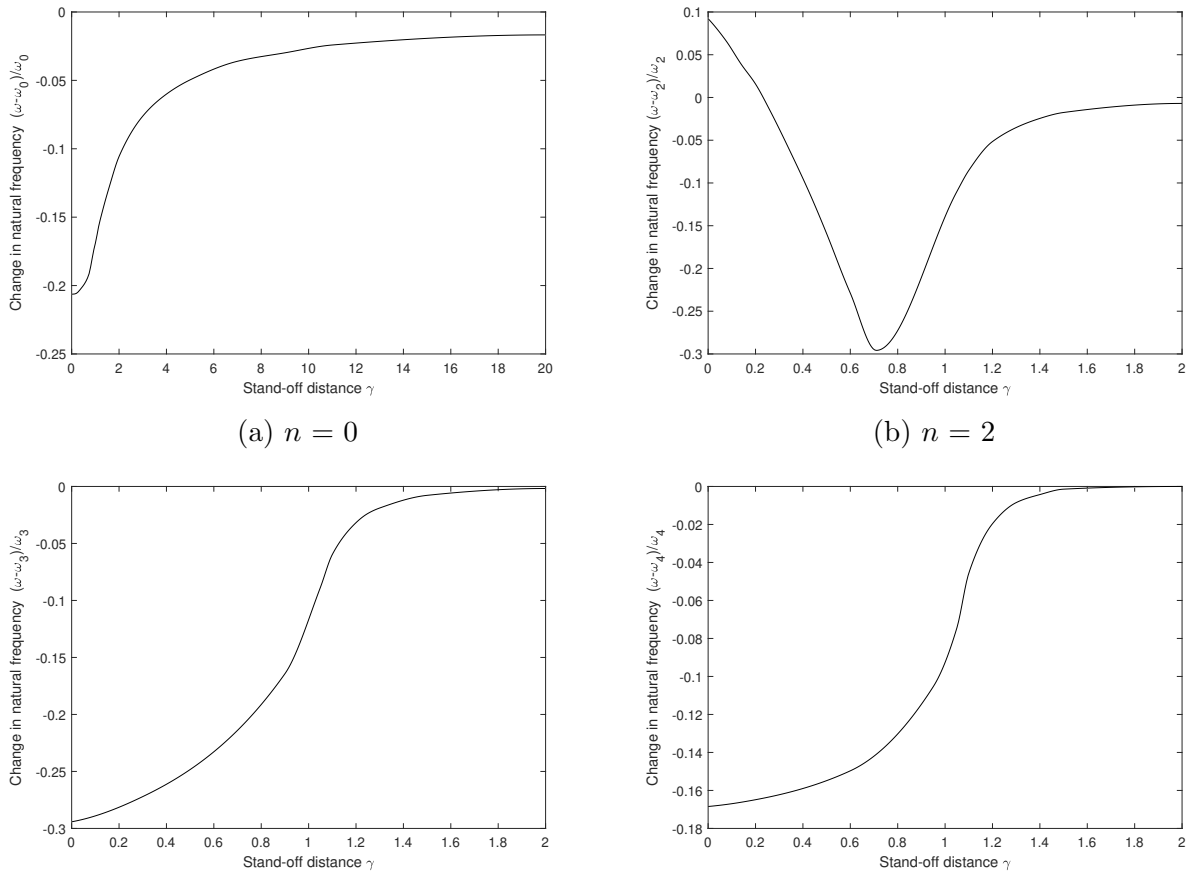

(a) $n = 0$ (b) $n = 2$

(c) $n = 3$ (d) $n = 4$

Figure 5: The change in shape mode n natural frequency with increasing stand-off distance for four different modes of oscillation. The bubble has initial radius $R_0 = 25$ μm, initial potential $\phi_0 = \epsilon P_n(\cos\theta)$ where $\epsilon \ll 1$, θ is the angle between the position on the bubble surface and the r-axis, and $P_n(\cos\theta)$ is the Legendre polynomial of order n. The remaining parameters are the same as in figure 3.

Figure 5a shows the change in natural frequency of shape mode zero, representing volu-

metric oscillation, for different stand-off distances. As the initial distance between the bubble and the wall decreases, the natural frequency decreases. This is the effect of the flow between the bubble and the wall being inhibited by the wall, which has a greater impact the closer the bubble is to the wall. As the stand-off distance becomes large, the natural frequency tends to the natural frequency of a bubble in an infinite fluid. When the non-dimensional stand-off distance $\gamma = 50$, the natural frequency of shape mode zero oscillation is within one percent of that in an infinite fluid.

As the stand-off distance increases above $\gamma = 10$, the change in natural frequency begins to increase at a linear rate. Below this point, the natural frequency changes at a non-linear rate. It is below $\gamma = 5$ that the natural frequency begins to rapidly decrease, signifying the growing impact of the wall as the distance between the bubble and wall decreases. When the bubble is fixed to the wall for $\gamma \leq 1$, the natural frequency continues to decrease at the same rate before tailing off around $\gamma = 0.5$. At $\gamma = 0$, the effect of the wall is at a maximum and so the natural frequency is at its minimum. This corresponds to a 21 percent decrease in natural frequency compared to a bubble in an infinite fluid.

Figure 5b shows the change in natural frequency of shape mode two oscillation for different stand-off distances. For stand-off distances greater than $\gamma = 1.75$, the natural frequency of mode two oscillation is within one percent of an equivalent bubble in an infinite fluid. The change in frequency slowly increases and tends towards zero as the stand-off distance increases beyond $\gamma = 1.75$. The wall has a significantly smaller effect on the oscillation frequency of shape mode two, when compared to mode zero oscillation, for $\gamma \geq 1$.

When the stand-off distance decreases below $\gamma = 0.7$, the change in natural frequency begins to increase. It continues to steadily increase until it reaches a maximum at $\gamma = 0$ of a 9 percent increase compared to a bubble in an infinite fluid. This can be explained by the effect of the fixed contact line on the shape mode two oscillation. When $\gamma = 0$, the bubble is a hemisphere resting on the wall. In this case, the fixed contact line is located at an antinode of oscillation for shape mode two. Enforcing the fixed contact line is analogous to imposing fixed boundary conditions to a freely oscillating system. This in turn leads to an increased natural frequency due to a reduced amplitude of oscillation.

Figures 5c and 5d show the change in natural frequency of shape modes three and four oscillation for different stand-off distances respectively. Both figures show similar behaviour, with the change in natural frequency approaching that of a bubble in an infinite fluid as γ increases. The natural frequency of shape mode oscillation is within one percent of an equivalent bubble in an infinite fluid when the stand-off distance is greater than $\gamma = 1.44$ for mode three, and $\gamma = 1.28$ for mode four.

In both cases, as the stand-off distance increases, the change in natural frequency increases. The change in natural frequency of shape mode three increases at a much greater rate than shape mode four, when the stand-off distance is between $\gamma = 0$ and $\gamma = 0.8$. For both figures, the decrease in natural frequency is at its maximum when $\gamma = 0$. Shape mode three oscillation sees a 29 percent decrease, and shape mode four oscillation sees a 17 percent decrease at this point.

Comparing the different modes, we can make a number of observations. Firstly, for

stand-off distances greater than approximately $\gamma = 1.2$, we note that as the mode number increases, the effect of the wall on the natural frequency decreases. This can be seen by comparing the exact stand-off distance at which the natural frequency of the mode is within one percent of a bubble in an infinite fluid. For mode zero this value is $\gamma = 50$, for mode two $\gamma = 1.75$, mode three $\gamma = 1.44$, and mode four $\gamma = 1.28$.

As the mode number increases, there is a decrease in natural frequency at $\gamma = 0$ when considering the even and odd modes separately. This implies that there are two separate behaviours for the even and odd modes. This trend can be seen in figure 6 in which the change in natural frequency is plotted against the increasing shape mode number. We see that the odd modes are more affected by the presence of the wall, as there is a larger decrease in natural frequency for odd modes compared to their even counterparts.

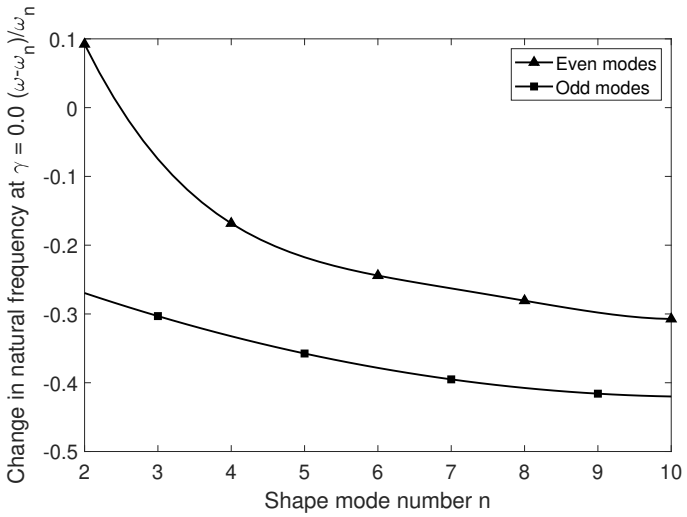

Figure 6: The change in natural frequency at a stand-off distance $\gamma = 0$ for increasing mode number. The even and odd modes are separated due to their different behaviours. The parameters are the same as in figure 5.

3.3 Shear stress generated on a rigid boundary by different modes of oscillation

Here, we consider a bubble initially at equilibrium with radius $R_0 = 25$ μm, at a nondimensional stand-off distance from a rigid boundary of $\gamma = 1.3$ and $\gamma = 5.0$. The remaining parameters are the same as defined in table 1. The stand-off distance $\gamma = 1.3$ represents the behaviour of the bubble when it exists close to the wall, and the stand-off distance $\gamma = 5.0$ represents the behaviour of the bubble far away from the wall.

For both cases, the initial potential prescribed to the surface of the bubble is chosen to be $\phi_0 = \phi_a P_n(\cos\theta)$, where ϕ_a is the dimensionless amplitude of the potential distribution. To satisfy the constraint requiring the same initial kinetic energy for each modes, the size of the potential amplitude when $\gamma = 1.3$ is $\phi_a = 0.00692$, 0.00780, 0.00785, and 0.00787 for

modes zero, two, three, and four respectively. When $\gamma = 5.0$, the potential amplitude is ϕ_a = 0.00775, 0.00954, 0.00978, and 0.00991 for modes zero, two, three, and four respectively.

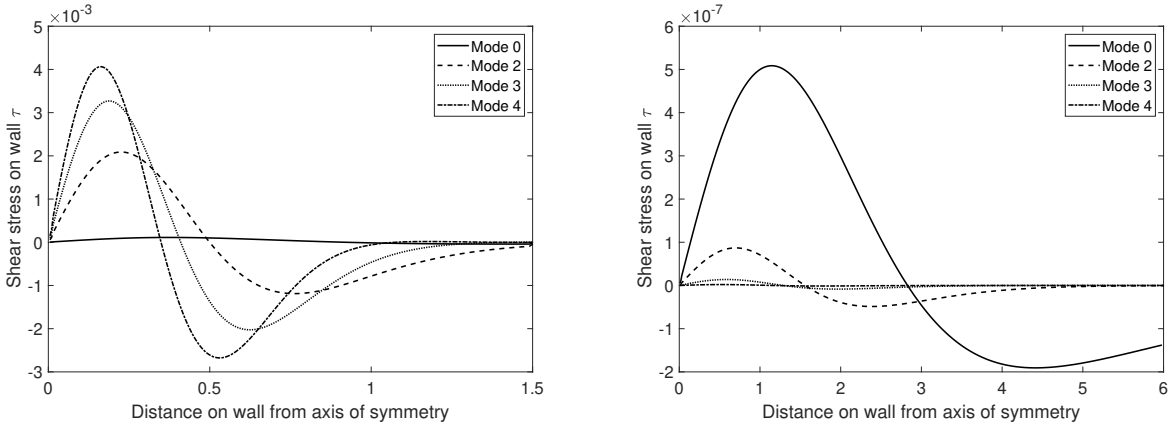

(a) $\gamma = 1.3$ (b) $\gamma = 5.0$

Figure 7: Comparison between the dimensionless shear stress generated on a rigid boundary by a bubble in shape mode zero, two, three and four oscillation at a stand-off distance of (a) $\gamma = 1.3$ and (b) $\gamma = 5.0$. The bubble has initial radius $R_0 = 25$ μm and dimensionless initial potential $\phi_0 = \phi_a P_n(\cos\theta)$, where in (a) ϕ_a = 0.00692, 0.00780, 0.00785 and 0.00787, and in (b) ϕ_a = 0.00775, 0.00954, 0.00978 and 0.00991 for modes zero, two, three and four, respectively. The remaining parameters are as in figure 3.

Figures 7a and 7b display the shear stress on a rigid boundary generated by different shape modes when the bubble is close to and far away from the boundary respectively. The shear stress distribution is chosen at the time that the maximum shear stress occurs. Observing figure 7a, it is clear that as the shape mode increases, so too does the maximum shear stress on the wall. Not only this, but the position of the maximum point moves closer to the axis of symmetry as the mode number increases. This could be explained by the fact that the width of the protrusion closest to the boundary decreases with increasing shape mode. For example, mode three is characterised by three protrusions of equal width, whilst mode four is characterised by four protrusions of equal width. The mode four protrusions have smaller width than those of mode three when both are compared on a bubble of the same size.

The maximum shear stress increasing with mode number may be explained by the speed of the protrusion closest to the wall. As the mode number increases, the frequency of shape mode oscillation increases, as does the speed of shape mode oscillation. The maximum occurs during the first oscillation, in which the protrusion closest to the boundary moves towards the boundary. As this protrusion dictates the behaviour of the shear stress, it follows that higher modes are associated with greater shear stress on the boundary due to the higher speeds. This is the case when the bubble is close to the wall where surface oscillations dominate the behaviour of the shear stress.

It can also be seen that as the mode number increases, the smaller the area the majority

of the shear stress acts upon. For example, mode four oscillation exhibits the largest shear stress close to the axis of symmetry, however when the distance from the axis exceeds 0.6, the other modes begin to have greater values. On the other hand, despite mode zero oscillation having the smallest values of shear stress near to the axis of symmetry, when the distance exceeds approximately 1.8, mode zero has the greatest effect on the wall. In this region beyond a distance of 1.8, the behaviour is essentially reversed, and the values of shear stress decrease with increasing mode number.

For a bubble close to a boundary, higher shape modes of oscillation lead to a concentration of shear stress towards the axis of symmetry. This leads to significant increases in the maximum shear stress on the wall; shape mode four has a maximum shear stress approximately 20 times larger than that of mode zero. For higher modes, the majority of the shear stress occurs in the area directly beneath the bubble. Beyond a distance of approximately 1.5 from the axis of symmetry, the effect of the shear stress is essentially negligible when compared to that in the inner region. This could greatly benefit applications such as targeted ultrasonic cleaning.

Observing figure 7b, it is clear that the maximum value of shear stress decreases with an increasing mode number. As with a bubble initiated close to a boundary, the position of the maximum value approaches the axis of symmetry when the mode number increases. Now, however, it is volumetric oscillation that drives the behaviour of the shear stress rather than surface oscillations.

As the bubble is further away from the boundary, it is no longer just the protrusion closest to the boundary that has the most significant impact. As the mode number increases, the amplitude of volumetric oscillation decreases. This explains why the maximum shear stress decreases as the mode number increases, given that volumetric oscillation is the driving force behind the generation of shear stress when the bubble is far away from the wall. Now, in contrast to the case with a bubble close to a wall, mode zero is by far the most effective shape mode to generate shear stress.

This implies that an approach with with two frequencies would be advisable to target both behaviours. This will ensure a more uniform cleaning and is in line with the approach used in industry.

3.4 Bubble shapes

The trends observed in figures 5 - 7 should have an effect on the shapes of the bubbles generated in these configurations. In order to observe these trends, we will consider three cases: a bubble initiated on a rigid boundary, close to a rigid boundary, and far away from a rigid boundary. To best contrast these behaviours, the three cases are taken to have stand-off distances of $\gamma = 0.0$, $\gamma = 1.3$, and $\gamma = \infty$ respectively. The specifications remain the same as in table 1, just with a larger initial potential amplitude. A larger potential amplitude is taken to better illustrate the changes to the bubble shapes.

The shapes at maximum expansion of modes three and four are compared to demonstrate the difference between odd and even modes. To conserve energy between cases, the dimensionless potential amplitude ϕ_a for mode three is taken to be $\phi_a = 0.0321$, 0.2550, and 0.0265 when $\gamma = \infty$, 1.3, and 0.0 respectively. For mode four, the potential amplitude is

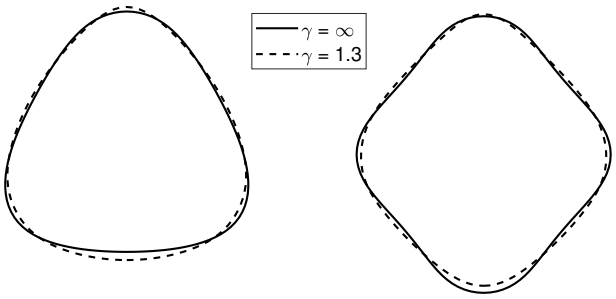

Figure 8: A comparison between the bubble shapes at maximum expansion for a bubble with initial radius $R_0 = 25$ μm close to a wall ($\gamma = 1.3$, dashed line), and far away from a wall ($\gamma = \infty$, solid line). Two cases are considered: mode three (left), and mode four (right). The dimensionless initial potential for mode three is $\phi_0 = \phi_a P_3(\cos\theta)$ with potential amplitude $\phi_a = 0.0321$ and 0.0255 for $\gamma = \infty$ and 1.3, respectively. For mode 4, $\phi_a = 0.0326$ and 0.0254 for $\gamma = \infty$ and 1.3, respectively. The remaining parameters are as in figure 3.

taken to be $\phi_a = 0.0326$, 0.2540, and 0.0251 when $\gamma = \infty$, 1.3, and 0.0 respectively. Figure 8 displays how the bubble shapes change with stand-off distance for modes three and four. Figure 9 compares how the bubble shapes change between modes for a bubble initiated on a wall and close to a wall.

Inspecting figure 8, we observe that mode three oscillation has a larger amplitude when the bubble is closer to the wall. This corresponds with the decreasing natural frequency as the bubble approaches the wall as in figure 5c. On the other hand, mode four displays very similar bubble shapes for both the close and far cases. As can be seen by comparing figures 5c and 5d, the natural frequency of mode four oscillation is less affected by the wall than mode three oscillation. Thus it follows that the wall should have less of an effect on the bubble shape. This trend is also reflected by the decreasing distance from the wall at which the natural frequency of increasingly higher shape modes of oscillation is within one percent of that of an equivalent bubble in an infinite fluid. Thus we would expect that the bubble shape at a fixed stand-off distance should be less affected by the wall as the mode number increases.

Inspecting figure 9, we observe the differences between the shapes at maximum expansion of mode three and mode four oscillation at stand-off distances of $\gamma = 0.0$ and $\gamma = 1.3$. When the stand-off distance $\gamma = 0.0$, the bubble is initially a hemisphere connected to the rigid boundary. As can be seen, the fixed point connecting the bubble to the wall occurs at a node of mode four oscillation, inhibiting the ability of the bubble to reach maximum expansion. On the other hand, the fixed point does not occur at a node of mode three oscillation, leaving the bubble more free to expand. This property is the reason for the two separate behaviours of the oscillation frequency of odd and even modes, as the inhibited oscillation of even modes

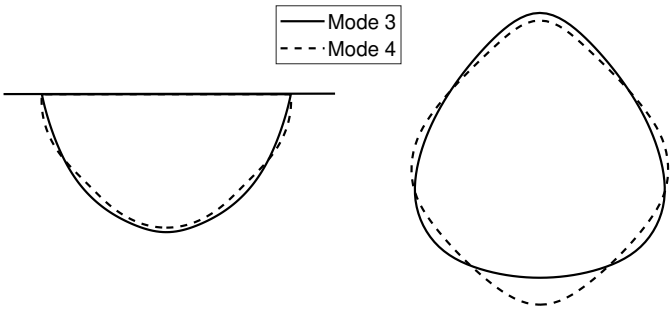

Figure 9: A comparison between the bubble shapes at maximum expansion for a bubble with initial radius $R_0 = 25$ μm of mode three (solid line) and mode four (dashed line) oscillation, considering a bubble initiated at a stand-off distance of $\gamma = 0.0$ (left) and $\gamma = 1.3$ (right). The initial potential for mode three is $\phi_0 = \phi_a P_3(\cos\theta)$ with dimensionless potential amplitude $\phi_a = 0.0255$ and 0.0265 for $\gamma = 1.3$ and 0.0, respectively. For mode 4, $\phi_a = 0.0254$ and 0.0251 for $\gamma = 1.3$ and 0.0, respectively. The remaining parameters are as in figure 3.

leads to a lower amplitude and hence higher frequency.

At a stand-off distance of $\gamma = 1.3$, the tip of the node closest to the rigid boundary is narrower than the equivalent case at $\gamma = \infty$. This corresponds with the narrower distribution of shear stress on the rigid boundary when the bubble is closer to the wall, as seen in figures 7a and 7b. Additionally, the tip of the mode four node is narrower than that of the mode three node, corresponding with the findings of figure 7a.

The shape mode three node closest to the wall has a larger amplitude than that of mode four. This is due to the higher frequency of mode four oscillation than mode three. The maximum shear stress generated on the wall, however, is larger for mode four than mode three. This indicates that the effect of the larger velocity associated with mode four oscillation makes up for the smaller amplitude of oscillation when compared with mode three. This explains the larger maximum shear stress generated on the wall by mode four oscillation than mode three, a trend which continues as the mode number increases.

3.5 Comparison with experimental observations

Having analysed the shear stress generated on a rigid boundary when the bubble is close and far away, we now consider the case of a bubble initiated on the wall. This is to compare with the experimental results of Vyas et al. [2020], in which a bubble attached to a rigid boundary is shown only cleaning the area in the immediate vicinity of the bubble (supplementary video d).

To compare with this case, the contact angle between the bubble surface and the wall is chosen to be $\theta_c = \pi/4$, translating to an initial stand-off distance of approximately $\gamma = 0.707$. The remaining parameters are the same as in previous cases, with the exception of the

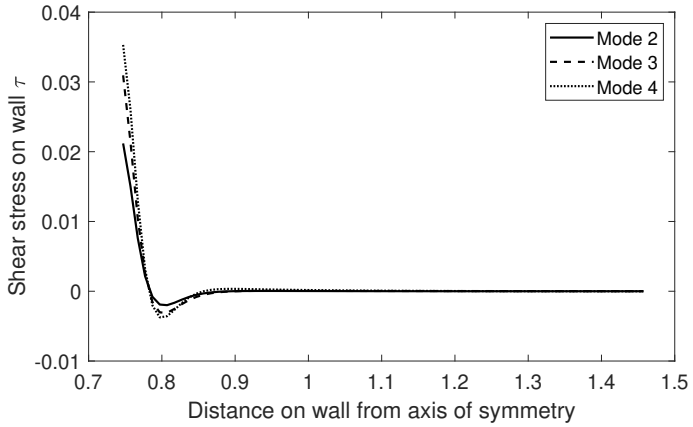

Figure 10: Dimensionless shear stress generated on a rigid boundary by a bubble located at a stand-off distance of $\gamma = 0.70$. Shape modes two, three and four are compared. The remaining parameters are the same as in figure 5, with dimensionless potential amplitude ϕ_a = 0.00470, 0.00475 and 0.00480 for modes two, three and four, respectively.

potential amplitude selected to be ϕ_a = 0.00470, 0.00475 and 0.00480 in order to conserve energy between modes.

As is seen in figure 10, shear stress is generated directly in the region near to the bubble surface. This agrees with experimental observations. Additionally, higher shape modes generate a larger maximum shear stress on the boundary. This suggests that higher shape modes should be targeted to maximise the removal of contaminants from a rigid boundary. The order of the maximum shear stress increases significantly as the stand-off distance decreases, so targeting higher shape modes located close to a rigid boundary should prove to be optimal for removal. The results from this paper for the behaviour of the natural frequency of shape mode oscillation at different stand-off distances can be used to more effectively target these higher shape modes near to a wall.

4 Conclusions

A numerical model is described for the shape mode oscillation of a bubble near to as well as connected to a rigid boundary. It is based on the boundary integral method, with the viscous effects modelled using viscous potential flow theory and the compressible effects using weakly compressible theory. The viscous stress at the boundary is approximated using boundary layer theory. Parametric studies are carried out for the natural frequency of shape modes and the shear stress at the rigid boundary in terms of the shape modes and the standoff distance of the bubble from the boundary. A series of new features have been noticed, which may be summarized as follows.

The natural frequency of shape mode oscillation of a bubble near a rigid boundary is decreased by the presence of the boundary. The wall effects decrease as the standoff distance increases, and the larger the mode number, the faster the wall effects decrease. The maximum decreases in the natural frequency for modes $k = 0$ (spherical mode), 2, 3, 4 are

21%, 30%, 29% and 14%.

As a bubble oscillates with shape modes either very close to or in contact with a rigid boundary, significant shear stress occurs only within approximately 1.5 R_{eq} from the axis of symmetry, with the maximum value of shear stress located within the image of the projection of the bubble onto the wall. The shear stress at the rigid boundary decreases when the standoff distance of the bubble from the boundary increases. The shear stress due to shape oscillation decreases faster with the standoff distance than that due to the volume oscillation of bubbles. The larger the shape mode the faster the shear stress decreases with the standoff distance.

In particular, the magnitude of the shear stress generated by the shape oscillation of a bubble very close to the rigid boundary is at least twenty times larger than that due to spherical oscillation with the same energy. This is because the shape mode oscillation of bubbles generates more local streaming and stress rather than that due to volume oscillation of a bubble at the same energy. This explains the dramatic cleaning effects of a bubble oscillating with shape modes in very close proximity to a rigid boundary, the experimental findings of Vyas et al. [2020], in which the bubble only cleans the area in close proximity to the bubble surface.

These results are consistent with the order analysis based on perturbation theory. The induced velocity due to shape mode k is $\mathcal{O}(r^{-(k+2)})$, decaying faster for a larger mode k. For the non-spherical shape modes, i.e. $k \geq 2$, the induced velocity decreases much faster than that of spherical oscillation ($k = 0$). The disturbance of shape oscillation to the flow decays much faster away from the bubble than that of spherical oscillation. As such, the wall effects for shape mode oscillation decrease with the standoff distance much faster than spherical oscillation; the higher the shape mode k the faster the decrease.

The shear stress distribution at the rigid boundary generated by shape mode k is $\mathcal{O}(r^{-3(k+3)})$ using equation 2.9, decaying faster with the standoff distance than the induced velocity. This confirms the local nature of the shear stress at the rigid boundary due to shape oscillation.

References

J. R. Blake and D. C. Gibson. Cavitation bubbles near boundaries. *Annual Review of Fluid Mechanics*, 19(1):99–123, 1987.

W. Lauterborn and T. Kurz. Physics of bubble oscillations. *Reports on Progress in Physics*, 73(10):106501, 2010.

C. D. Ohl, M. Arora, R. Dijkink, V. Janve, and D. Lohse. Surface cleaning from laser-induced cavitation bubbles. *Applied Physics Letters*, 89(7):074102, 2006.

G. L. Chahine, A. Kapahi, J. K. Choi, and C. T. Hsiao. Modeling of surface cleaning by cavitation bubble dynamics and collapse. *Ultrasonics Sonochemistry*, 29:528–549, 2016. ISSN 1350-4177.

F. Reuter, S. Lauterborn, R. Mettin, and W. Lauterborn. Membrane cleaning with ultrasonically driven bubbles. *Ultrasonics Sonochemistry*, 37:542–560, 2017. ISSN 1350-4177.

T. J. Mason. Ultrasonic cleaning: An historical perspective. *Ultrasonics Sonochemistry*, 29: 519–523, 2016.

N. Vyas, Q. X. Wang, K. A. Manmi, R. L. Sammons, S. A. Kuehne, and A. D. Walmsley. How does ultrasonic cavitation remove dental bacterial biofilm? *Ultrasonics Sonochemistry*, 67, 105112, 2020.

M. S. Plesset. On the stability of fluid flows with spherical symmetry. *J. Appl. Phys.*, 25 (96), 1954.

A. Prosperetti. Viscous effects on perturbed spherical flows. *Quart. Appl. Math.*, 34(339), 1977.

S. J. Shaw. The stability of a bubble in a weakly viscous liquid subject to an acoustic traveling wave. *Physics of Fluids*, 21(2):022104, 2009.

S. J. Shaw. Nonspherical sub-millimeter gas bubble oscillations: Parametric forcing and nonlinear shape mode coupling. *Physics of Fluids*, 29(12):122103, 2017.

A. A. Doinikov. Mathematical model for collective bubble dynamics in strong ultrasound fields. *The Journal of the Acoustical Society of America*, 116(2):821–827, 2004.

M. Guédra, C. Cornu, and C. Inserra. A derivation of the stable cavitation threshold accounting for bubble-bubble interactions. *Ultrasonics Sonochemistry*, 38:168–173, 2017. ISSN 1350-4177.

M. Guédra and C. Inserra. Bubble shape oscillations of finite amplitude. *Journal of Fluid Mechanics*, 857:681–703, 2018.

V. Garbin, D. Cojoc, E. Ferrari, E. Di Fabrizio, M. L. J. Overvelde, S. M. van der Meer, N. de Jong, D. Lohse, and M. Versluis. Changes in microbubble dynamics near a boundary revealed by combined optical micromanipulation and high-speed imaging. *Applied Physics Letters*, 90(11):114103, 2007.

A. A. Doinikov and A. Bouakaz. Theoretical investigation of shear stress generated by a contrast microbubble on the cell membrane as a mechanism for sonoporation. *The Journal of the Acoustical Society of America*, 128(1):11–19, 2010.

S. Roovers, T. Segers, G. Lajoinie, J. Deprez, M. Versluis, S. De Smedt, and I. Lentacker. The role of ultrasound-driven microbubble dynamics in drug delivery: From microbubble fundamentals to clinical translation. *Langmuir*, 35, 01 2019.

A. Maksimov. Splitting of the surface modes for bubble oscillations near a boundary. *Physics of Fluids*, 32, 102104, 2020.

D. D. Joseph and J. Wang. The dissipation approximation and viscous potential flow. *J. Fluid Mech.*, 505:365–377, 2004.

Q. X. Wang, W. Liu, C. Corbett, and W. R. Smith. Microbubble dynamics in a viscous compressible liquid subject to ultrasound. *Physics of Fluids*, 34, 012105, 2022.

Q. X. Wang and J. R. Blake. Non-spherical bubble dynamics in a compressible liquid. Part 1. Travelling acoustic wave. *Journal of Fluid Mechanics*, 659:191–224, 2010.

Q. X. Wang and J. R. Blake. Non-spherical bubble dynamics in a compressible liquid. Part 2. Acoustic standing wave. *Journal of Fluid Mechanics*, 679:559–581, 2011.

J. A. Tsamopoulos and R. A. Brown. Nonlinear oscillations of inviscid drops and bubbles. *Journal of Fluid Mechanics*, 127:519–537, 1983.

W. L. Nyborg. Acoustic streaming near a boundary. *J. Acoust. Soc. Am.*, 30:329–339, 1958.

Q. X. Wang and K. Manmi. Microbubble dynamics near a wall subjected to a travelling acoustic wave. *Physics of Fluids*, 26, 032104, 2014.

Q. X. Wang. Local energy of a bubble system and its loss due to acoustic radiation. *Journal of Fluid Mechanics*, 797:201–230, 2016.

A. J. Szeri, B. D. Storey, A. Pearson, and J. R. Blake. Heat and mass transfer during the violent collapse of nonspherical bubbles. *Physics of Fluids*, 15(9):2576–2586, 2003.

D. Fuster and F. Montel. Mass transfer effects on linear wave propagation in diluted bubbly liquids. *Journal of Fluid Mechanics*, 779:598–621, 2015.

S. J. Lind and T. N. Phillips. The effect of viscoelasticity on a rising gas bubble. *Journal of Non-Newtonian Fluid Mechanics*, 165(15):852–865, 2010. ISSN 0377-0257.

S. J. Lind and T. N. Phillips. The influence of viscoelasticity on the collapse of cavitation bubbles near a rigid boundary. *Theoretical and Computational Fluid Dynamics*, 26:245–277, 2012.

S. J. Lind and T. N. Phillips. The effect of viscoelasticity on the dynamics of gas bubbles near free surfaces. *Physics of Fluids*, 25(2):022104, 2013.

Q. X. Wang, W. K. Liu, A. M. Zhang, and Y. Sui. Bubble dynamics in very close to a rigid boundary. *Interface Focus*, 5(5), 20150048, 2015.

B. Y. Ni, A. M. Zhang, and G. X. Wu. Numerical and Experimental Study of Bubble Impact on a Solid Wall. *Journal of Fluids Engineering*, 137(3), 03 2015. ISSN 0098-2202. 031206.

Y. Shikhmurzaev. Capillary flows with forming interfaces. *Chapman and Hall/CRC*, 09 2007.

Q. X. Wang, W. Liu, D. Leppinen, and Walmsley D. Microbubble dynamics in a viscous compressible liquid near a rigid boundary. *IMA Journal of Applied Mathematics*, 84(4): 696–711, August 2019. ISSN 0272-4960.